

## Highly Resolved Self-Excited Density Waves in a Complex Plasma

M. Schwabe,\* M. Rubin-Zuzic, S. Zhdanov, H. M. Thomas, and G. E. Morfill

Max-Planck-Institut für extraterrestrische Physik, D-85740 Garching, Germany

(Received 27 April 2007; published 30 August 2007)

Experimental results on self-excited density waves in a complex plasma are presented. An argon plasma is produced in a capacitively coupled rf discharge at a low power and gas pressure. A cloud of microparticles is subjected to effective gravity in the range of 1–4 g by thermophoresis. The cloud is stretched horizontally (width/height  $\approx$  45 mm/8 mm). The critical pressure for the onset of the waves increases with the temperature gradient. The waves are propagating in the direction of the ion drift. The wave frequency, phase velocity, and wavelength are measured, and particle migrations affected by the waves are analyzed at a time scale of 1 ms/frame and a subpixel space resolution.

DOI: 10.1103/PhysRevLett.99.095002

PACS numbers: 52.27.Lw, 52.35.Fp, 52.35.Mw

In this Letter we address wave patterns observed in complex plasmas [1]. Self-excited waves (autowaves) are an important element of self-organization in nature [2]. For instance, they are observed in plastic deformation flows [3] and hydrothermal flows [4] or formed by striations in discharges [5]. Rhythmic patterns of mobile marine sandy beds and sand ripples are usual in deserts and along coasts [6,7]. The common feature of these phenomena is that the medium is in an active state due to external tension or has an active agent (wind, water, plasma ions, etc.).

Complex plasmas are low pressure low temperature plasmas containing microparticles. These particles can be visualized individually with a laser beam, the light of which is scattered by the particles, and then recorded with a CCD camera. The particles, collecting electrons and ions from the surrounding plasma, acquire a strong negative charge and are levitated against gravity, e.g., in the sheath above the lower rf electrode [1] or in the strong electric field of dc discharge striations [8]. Under gravity conditions it is possible to levitate only a limited number of layers; therefore, the cloud practically has a two-dimensional structure. Under microgravity conditions, e.g., in experiments on board the International Space Station [9,10] or in parabolic flight experiments [11,12], essentially three-dimensional structures are formed. In ground-based experiments it is possible to elevate dense multilayer particle clouds vertically by thermophoresis [13,14].

Dense clouds of particles are of great interest because they reveal clearly a very special type of dynamical activity involving excitation of *density waves*, which have been observed experimentally using dc discharges (see, e.g., [11,15]) and rf discharges (see, e.g., [10,12]). In this study we investigate an rf plasma. The experiments on board the International Space Station [10] and in parabolic flight experiments [12] were performed under similar discharge conditions as ours in parallel plate rf discharges; the main difference was the size of the injected microparticles (6.8  $\mu\text{m}$  and a mix of 3.4 and 6.8  $\mu\text{m}$  in [12,10], respectively). However, in [10] no self-excitations were reported; the waves were excited externally (see also [9]). Piel *et al.*

[12] claimed the presence of an oblique wave propagation in fast ion flows, which takes place in the sheath region. In both cases, density waves were treated as linear (with some modifications of the dust acoustic waves), taking into account particle collisions. Nonlinear wave patterns observed in the experiments were not explained, as it was not possible to trace particle trajectories inside the dense clouds at the selected level of imaging rates.

In this study we recorded density waves at a rate 40 and 10 times faster than that chosen in [10,12], respectively. This allows us to perform investigations at the kinetic level with smaller particles and 3–4 times faster waves. We performed our experiments in a PK-3 Plus chamber, employing a symmetrically driven parallel plate capacitively coupled rf discharge, shown schematically in Fig. 1. The lower electrode is heated, so that an adjustable temperature gradient pointing downward is created in the chamber. We used argon gas at pressures between 10 and 40 Pa at a very small symmetrical gas flow with a typical peak-to-peak voltage of 30 V at a power of 17 mW. Under these conditions, the amount of disruption of the observed waves,

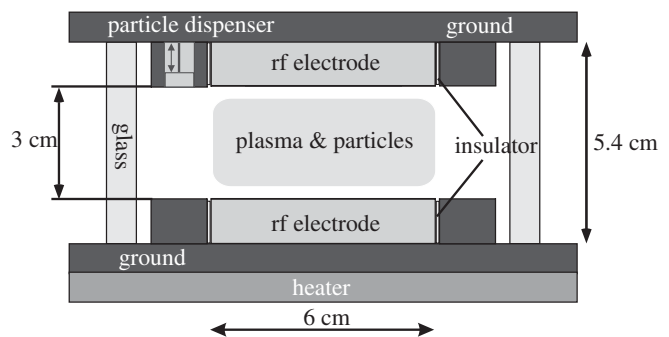


FIG. 1. Cross section through the setup. The parallel plate discharge is symmetrically driven by two rf electrodes, which have a diameter of 6 cm and are separated by 3 cm. They are surrounded by a ceramic insulator and a grounded ring of 9 cm diameter and 1.3 cm width. The heater, shown only schematically, consists of 8 evenly distributed resistors. The upper electrode is cooled with two 40  $\times$  40 mm case fans (omitted in the figure).

such as bifurcations and bending of the wave ridges, was minimal. Using a microparticle dispenser mounted into the upper grounded ring, we inserted melamine-formaldehyde particles with a diameter of  $1.280 \pm 0.056 \mu\text{m}$  and a mass density of  $1510 \text{ kg/m}^3$  into the chamber. Additionally, a relatively small number of bigger particles was present in the chamber, presumably agglomerates. The bigger particles do not influence the dynamics of the density waves. The microparticles were suspended at a certain height against gravity by electric and thermophoretic forces, and were illuminated with a vertically expanded sheet of diode laser light. We recorded the light scattered by the microparticles at a right angle using a Photron Fastcam-1024 PCI camera with a frame rate of 1000 fps and a spatial resolution of 1 Mpixel at  $45.6 \mu\text{m}/\text{pixel}$ .

When the temperature gradient was increased, the levitation height of the particles also increased. At higher pressures, a uniform microparticle cloud was levitated in the chamber, its position depending on the temperature gradient. When the gas pressure was then lowered to a “critical” level, self-excited density waves appeared. Figure 2 shows that the critical pressure increases with the temperature gradient in a domain where the thermophoretic force acting on the particles exceeds gravity (see top axis in Fig. 2), so that the *effective gravity*  $\vec{g}_{\text{eff}} = \vec{g} + \vec{F}_{\text{th}}/m$  is directed oppositely to  $\vec{g}$ . The particle cloud thus occupies the upper part of the chamber and is compressed by the thermophoretic force [Fig. 2(b)], in analogy to the compression of the objects in [3], which developed plastic flow zones. In the regime where the waves are excited, the observed growth in  $P_{\text{crit}}$  is easy to explain assuming that

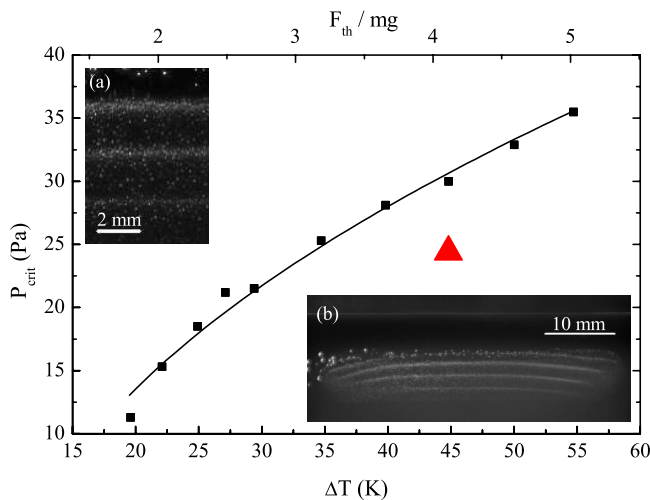


FIG. 2 (color online). Critical pressure for the onset of self-excitations versus the temperature difference between the electrodes. The top axis shows values of the normalized thermophoretic force calculated by using [14] (at a fixed electrode separation  $F_{\text{th}} \propto \Delta T$ ). Fit (solid line):  $P/P_0 = \sqrt{F_{\text{th}}/mg - 1 + \epsilon^2} - \epsilon$ ,  $P_0 = 21 \text{ Pa}$ ,  $\epsilon = 0.31$ . (Insets) Nonlinear wave pattern corresponding to the particular case of self-excitations discussed in details in the text (red triangle in the plot): (a) Central part of the image. (b) Entire cloud.

the waves are triggered by the streaming ion instability (with a growth rate of  $\gamma \propto v_i - v_*$  [15,16], where  $v_i = \mu E$  is the ambipolar diffusion speed,  $\mu \propto P^{-1}$  is the ion mobility, and  $v_*$  is the parameter from [15]) and stabilized by particle-gas friction; hence  $v_i - v_* \propto P$  at the instability threshold. From the force balance  $F_{\text{th}} - mg \approx Z_d |e| E_{\text{crit}}$ , we obtain the ratio  $F_{\text{th}}/mg$  as a polynomial function of  $P$ , assuming a constant  $Z_d$  and  $v_*$  in our range of parameters. Fitting (see Fig. 2) supports this assumption. The density waves propagate in the direction of effective gravity, which is also the direction of the ion drift.

Figure 3 (top) shows the periodgram taken over all 2000 still pictures registered during the experiment. Each vertical column in this picture (corresponding to a fixed time moment) was plotted by averaging over a 4.56 mm wide horizontal area of the central part of the image [see Fig. 2(a)]. Analyzing this diagram, first we fixed general regions of the wave ridges by plotting contour lines of intensity, and then defined positions of each “wave ridge” as an ensemble of brightest pixels in the corresponding area. From this data, we determined the distributions of wave parameters that are shown in the bottom part of Fig. 3. We determined the means of the data by fitting a robust Gaussian to the smoothed histograms. The average phase velocity turns out to be  $\langle v \rangle = 56 \pm 4 \text{ mm/s}$ , the average wave period is  $\langle dt \rangle = 28.8 \pm 0.9 \text{ ms}$ , and the wavelength is  $\langle \lambda \rangle = 1.73 \pm 0.05 \text{ mm}$ . (The error in the phase velocity stems from the linear fit, the error in the period from pixel noise, and the error in the wavelength from the camera resolution.) The phase velocity changes slightly with height ( $< 20\%$ ), while the period remains practically the same. With the velocity of 5.6 cm/s, the waves are faster than those examined in [12], which had a

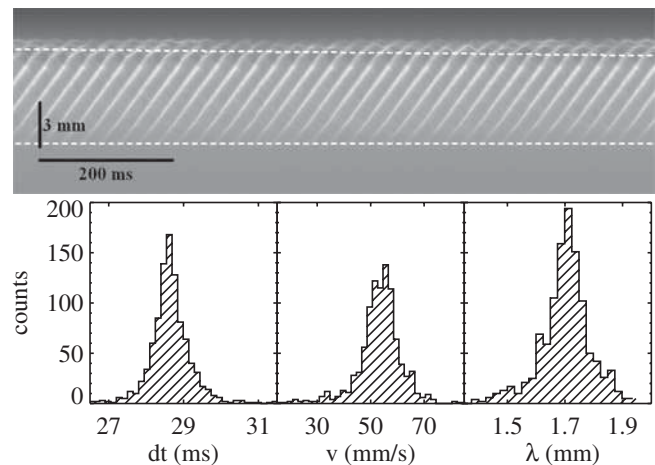


FIG. 3. (Top) Periodgram of the waves. The plot abscissa corresponds to time, the ordinate to height and the brightness to the renormalized sum of all pixel intensities in a 4.56 mm wide central region [Fig. 2(a)]. The horizontal dashed lines mark the boundaries of the plot area used for analysis. (Bottom) Histograms of the wave parameters determined from the intensity plot: period, phase velocity, and wavelength.

phase velocity of 1.6 cm/s. While tracing particle positions from one consecutive frame to another, we used only those tracks which contained more than 20 positions to ensure that traced particles are moving along the same plane. Only these tracks are used in the further analysis. Particles are “lost” from the viewing plane of the laser sheet mainly due to enhanced scattering on the denser wave ridges. For convenience we divide all the identified tracks into two groups. Longer trajectories crossing at least several ridges will be termed below as “well resolved” (about 130 events). They can serve as a probe of either a long-range or an in-front wave field. The remaining trajectories (about 2700 events) often broke off at wave fronts and formed a halo underneath the wave ridges. Hence, they are natural (and statistically well-defined) tests of the out-of-front field structure. We calculated the errors arising from pixel noise [17] and from fluctuations in the background (plasma) emission. The former error is less than 3%; the latter does not exceed 2%. An additional source of errors stems from statistics. These errors are of the order of 10% or less. Therefore, the expected maximal error does not exceed 15%.

When the particles are interacting with the waves (as a typical example see Fig. 4) they are captured by the wave field, drift backwards relatively slowly inside a ridge, then escape and relax back to their original position. These stages are repeated quasiperiodically. The drift stage corresponds to resonant interaction (“Landau acceleration”). Sometimes the particle is even carried along with the wave, but this is a rather weak process under our experimental conditions (Fig. 4). Chaotic or convective type motions of particles are very weak in the center of the cloud, though amplified toward the edges, where (relatively feeble) circulations exist, quite similar to those observed in [18]. Below we consider only the central part, which is free of circulations.

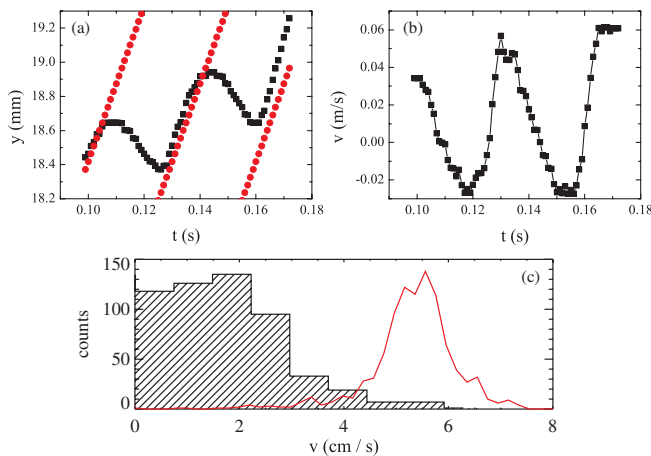


FIG. 4 (color online). (a) Resonant particle trajectory (black squares), wave front positions (red dots), and (b) particle velocity. (c) Histogram of velocities of well-resolved particles and the wave speed distribution (red line).

The force acting on the particles can be calculated using the relationship  $F_{\text{net}} = ma + \gamma mv$ , where  $m$  is the mass,  $a$  the acceleration,  $\gamma$  the Epstein drag coefficient [19] ( $\gamma = 236 \text{ s}^{-1}$  under our conditions), and  $v$  is the velocity. Figure 5 shows the result of the calculations taken in the same phase of the waves with the well-resolved particles (long tracks) and with all traced particles (mainly short tracks). In both cases, a periodical rise and fall in the force due to the periodic passage of the wave is clearly observable. The mean force in the second case is less than that calculated with the long-track particles, mostly because of the tracking problems mentioned above. For comparison we superimposed this plot with the force extracted from the trajectory of the resonant particle in Fig. 4 in the same phase. A movie showing the force in different wave phases and demonstrating the upward propagation of the wave is available online [20]. The total mean of the force irrespective of the wave phase (the dashed line in Fig. 5) turns out to be nonzero and increases in magnitude with height. The distribution of this mean field is fitted well by the line  $F = -\Omega_0^2 m(y - y_0)$ , where  $\Omega_0$  is the angular frequency (the spring constant) and  $y_0$  is the rest position. We measured  $\Omega_0 = 56 \pm 4 \text{ s}^{-1}$ .

An important question is the origin of the forces experienced by the particles inside a wave ridge. Using the model for the thermal conductivity for two-component materials described in [21], we calculated the expected variation in the thermophoretic force due to the presence of the microparticles as  $\Delta F_{\text{th}}/F_{\text{th}} \sim 10^{-7}$ . The additional

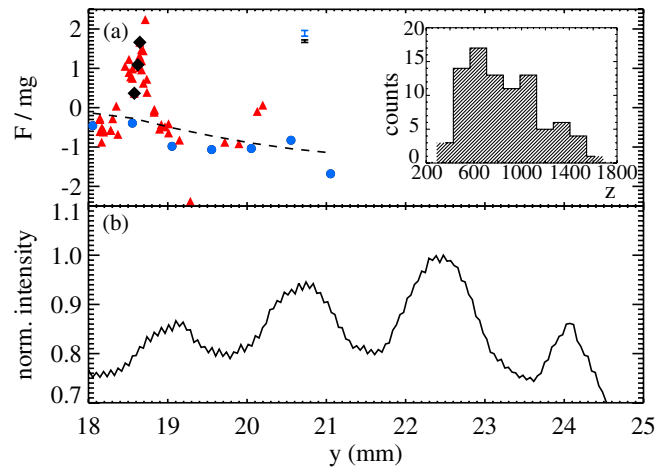


FIG. 5 (color online). (a) Net force acting on the particles in one phase of the wave as a function of height above the lower electrode: red triangles, well-resolved particles; blue dots, current mean force acting on all traced particles; dashed line, total mean of all traced particles; black diamonds, force-field calculated along the trajectory of the resonant particle. Corresponding error bars are shown atop. (Inset) Renormalized charge distribution of well-resolved particles calculated with Eq. (1). (b) Positions of wave ridges in the same phase taken from Fig. 3 vs height above the lower electrode. Note that the positions of force peaks (a) are shifted backward compared to the maxima of the emission intensity (b).

force due to particle overheating [22] is also very small:  $F_{\text{oh}}/F_{\text{th}} \sim 10^{-4}$  for our experimental conditions. Hence, the expected variation of the thermophoretic force caused by the influence of the microparticles is negligible. We showed earlier that the waves are excited when the electric field exceeds a critical value  $E_{\text{crit}}$ , and that the collective excitations are controlled by particle fluxes and energy conservation. The particle flux can be characterized by a simple balance taken forward (subscript 1) and backward (2) of the wave front:  $n_1(u - v_1) - n_2(u - v_2) + \frac{d}{dt} \times (nL) = 0$ , where  $n_{1(2)} = 3/(4\pi\Delta_{1(2)}^3)$  are the particle densities,  $\Delta_{1(2)}$  the particle separations, and  $v_{1(2)}$  the particle velocities,  $u$  is the wave velocity defined above (see Fig. 3), and  $nL$  is the particle density inside the wave ridge multiplied by the width of the ridge. By using tracing results we estimate (in a domain  $18 \text{ mm} < y < 19 \text{ mm}$  corresponding to the peak force in Fig. 5):  $\Delta_1 = 173 \text{ } \mu\text{m}$ ,  $\Delta_2 = 295 \text{ } \mu\text{m}$ , and the averaged (unperturbed) particle separation  $\langle \Delta \rangle = 232 \text{ } \mu\text{m}$ . Using these values we obtain  $n_1 = 4.6 \times 10^{10} \text{ m}^{-3}$ ,  $n_2 = 9.3 \times 10^9 \text{ m}^{-3}$ , and the averaged cloud density  $\langle n \rangle = 1.9 \times 10^{10} \text{ m}^{-3}$ , so that the compression factor equals:  $(n_1 - \langle n \rangle)/\langle n \rangle \approx 1.4$ . Under these conditions, the dust acoustic speed [23] is  $c_{\text{DAW}} = 3.7 \text{ cm/s}$ , which yields a Mach number  $M = u/c_{\text{DAW}} = 1.5$ . This confirms that the waves are really nonlinear.

The particle energy balance, assuming a simple model of symmetric screening [24,25], leads to a relationship for the “normalized particle charge”:

$$z \equiv \frac{Z_d \lambda_i}{\langle \Delta \rangle} = \left( \frac{4\pi\epsilon_0 m_d (u - v_1)^2 - (u - v_2)^2}{6\langle \Delta \rangle^2 e^2 (\Delta_2^{-3} - \Delta_1^{-3})} \right)^{1/2}, \quad (1)$$

where  $\lambda_i$  is the ion screening length. Here index 1,2 designates the particle positions outside, inside the wave ridges, respectively. The inset in Fig. 5 shows the distribution of  $z$  for the well-resolved particles. By fitting a robust Gaussian to the data we find a mean value of  $\langle z \rangle = 871 \pm 87$  at a confidence level of 95%.

To estimate plasma parameters we extrapolated results of Langmuir probe measurements performed under similar conditions in [26]. An electron temperature  $T_e$  of 3–4 eV was measured; therefore, we use  $T_e = 3.5 \text{ eV}$ . Extrapolating results of measurements in the central part of the chamber yields an estimate of the ion density of  $n_i = 2 \times 10^{14} \text{ m}^{-3}$  ( $4 \times 10^{14} \text{ m}^{-3}$  according to simulations [10]) for our conditions. Then, using relationship (1) we obtain  $Z_d \approx 2300$  for the particle charge, and  $H_{\text{max}} = Z_d n_1/n_i \approx 0.5$  for the Havnes parameter [27]. Note that the orbit motion limited theory [24,25] predicts a charge of  $Z_d = 2800$  ( $H = 0.5$ )—3600 ( $H = 0$ ). The drift motion limited theory [28], taking into account collisions, yields a charge of  $Z_d = 2200$ , while radial motion theory [29] predicts a charge of  $Z_d = 640$ . Therefore, our result is well within the theoretically expected range, and the simple explanation of the wave excitation seems feasible.

Using the charge  $Z_d = 2300$ , we estimate the strength of the total electric field acting on the particles inside the

wave ridges. From Fig. 5 we obtain  $F_{\text{max}}/mg \approx 2.5$  and thus  $E_{\text{max}} = (F_{\text{max}} - F_{\text{th}} + mg)/(-|e|Z_d) \approx 22 \text{ V/m}$ .

In conclusion, we investigated nonlinear highly resolved wave structures, self-excited in a complex plasma under the action of thermophoresis. We measured the wavelength, frequency, and phase velocity of the waves as well as the propagation and magnitude of the forces acting on the microparticles. We conclude that the self-excitation is due to the free energy in plasma ions drifting relative to the microparticles and explained the observed pressure dependence of the excitation threshold. The derived charge of the microparticles agrees well with that calculated using known theories.

The authors would like to acknowledge valuable discussions with H. Rothermel, U. Konopka, S. Khrapak, W. Bunk, and R. Pompl. This research was funded by “Das Bundesministerium für Wirtschaft durch das Zentrum für Luft- und Raumfahrt e.V. (DLR) unter dem Förderkennzeichen 50 WB 0203.”

\*schwabe@mpe.mpg.de

- [1] H. M. Thomas and G. E. Morfill, *Nature (London)* **379**, 806 (1996).
- [2] V. A. Vasiliev *et al.*, *Autowave Processes in Kinetic Systems* (VEB Deutscher Verlag der Wissenschaften, Berlin, 1987).
- [3] L. B. Zuev *et al.*, *Russ. Phys. J.* **44**, 169 (2001).
- [4] N. Garnier and A. Chiffaudel, *Phys. Rev. Lett.* **86**, 75 (2001).
- [5] J. Krása *et al.*, *J. Phys. D: Appl. Phys.* **7**, 2541 (1974).
- [6] S. J. M. H. Hulscher and C. M. Dohmen-Janssen, *J. Geophys. Res.* **110**, F04S01 (2005).
- [7] H. Nishimori and N. Ouchi, *Phys. Rev. Lett.* **71**, 197 (1993).
- [8] V. E. Fortov *et al.*, *JETP Lett.* **64**, 92 (1996).
- [9] A. P. Nefedov *et al.*, *New J. Phys.* **5**, 33 (2003).
- [10] S. Khrapak *et al.*, *Phys. Plasmas* **10**, 1 (2003).
- [11] M. Thoma *et al.*, *Microgravity Sci. Technol.* **18**, 47 (2006).
- [12] A. Piel *et al.*, *Phys. Rev. Lett.* **97**, 205009 (2006).
- [13] W. Cawood, *Trans. Faraday Soc.* **32**, 1068 (1936).
- [14] H. Rothermel *et al.*, *Phys. Rev. Lett.* **89**, 175001 (2002).
- [15] V. I. Molotkov *et al.*, *JETP* **89**, 477 (1999).
- [16] V. E. Fortov *et al.*, *Phys. Plasmas* **7**, 1374 (2000).
- [17] C. A. Knapek *et al.*, *Phys. Rev. Lett.* **98**, 015004 (2007).
- [18] M. Rubin-Zuzic *et al.*, *New J. Phys.* **9**, 39 (2007).
- [19] P. Epstein, *Phys. Rev.* **23**, 710 (1924).
- [20] <http://www.mpe.mpg.de/~mschwabe/waves.html>.
- [21] J. Wang *et al.*, *Int. J. Heat Mass Transfer* **49**, 3075 (2006).
- [22] G. Swinkels *et al.*, *J. Appl. Phys.* **88**, 1747 (2000).
- [23] P. K. Shukla, *Phys. Plasmas* **10**, 1619 (2003).
- [24] J. D. Swift and M. R. J. Schwar, *Electrical Probes for Plasma Diagnostics* (ILIFFE Books, London, 1970).
- [25] T. Matsoukas and M. Russel, *J. Appl. Phys.* **77**, 4285 (1995).
- [26] M. Klindworth *et al.*, *J. Phys. D* **39**, 1095 (2006).
- [27] O. Havnes *et al.*, *J. Geophys. Res.* **89**, 10 999 (1984).
- [28] G. E. Morfill *et al.*, *New J. Phys.* **8**, 7 (2006).
- [29] R. Kennedy and J. Allen, *J. Plasma Phys.* **67**, 243 (2002).